# Compact Open-Path Sensor for Fast Measurements of $CO_2$ and $H_2O$ using Scanned-Wavelength Modulation Spectroscopy with *1f*-Phase Method

**Xiang Li** [1] **, Feng Yuan** [2]**, Mai Hu** [2]**, Bin Chen** [2]**, Yabai He** [2]**, Chenguang Yang** [3]**, Lifang Shi** [4] **and Ruifeng Kan** [2,5,]***

[1] College of Environmental Science and Optoelectronic Technology, University of Science and Technology of China, Hefei 230026, China; xlee@aiofm.ac.cn

[2] Key Laboratory of Environmental Optics and Technology, Anhui Institute of Optics and Fine Mechanics, Chinese Academy of Sciences, Hefei 230031, China; fyuan@aiofm.ac.cn (F.Y.); maihu@aiofm.ac.cn (M.H.); bchen@aiofm.ac.cn (B.C.); yabaihe@hotmail.com (Y.H.)

[3] Institute of Deep Sea Science and Engineering, Chinese Academy of Sciences, Sanya 572000, China; cgyang@aiofm.ac.cn

[4] Institute of Optics and Electronics, Chinese Academy of Sciences, Sichuan 610200, China; shilifang@ioe.ac.cn

[5] State Key Laboratory of Applied Optics, Changchun Institute of Optics, Fine Mechanics and Physics, Chinese Academy of Sciences, Changchun 130033, China

***** Correspondence: rfkan@ciomp.ac.cn

check for updates

**Abstract:** We report here the development of a compact, open-path $CO_2$ and $H_2O$ sensor based on the newly introduced scanned-wavelength modulation spectroscopy with the first harmonic phase angle (scanned-WMS-θ*1f*) method for high-sensitivity, high temporal resolution, ground-based measurements. The considerable advantage of the sensor, compared with existing commercial ones, lies in its fast response of 500 Hz that makes this instrument ideal for resolving details of high-frequency turbulent motion in exceptionally dynamic coastal regions. The good agreement with a commercial nondispersive infrared analyzer supports the utility and accuracy of the sensor. Allan variance analysis shows that the concentration measurement sensitivities can reach 62 ppb $CO_2$ in 0.06 s and 0.89 ppm $H_2O$ vapor in 0.26 s averaging time. Autonomous field operation for 15-day continuous measurements of greenhouse gases ($CO_2/H_2O$) was performed on a shore-based monitoring tower in Daya Bay, demonstrating the sensor's long-term performance. The capability for high-quality fast turbulent atmospheric gas observations allow the potential for better characterization of oceanographic processes.

**Keywords:** in-situ sensors; rapid detection; atmospheric gases; costal environment; carbon dioxide; water vapor

## 1. Introduction

Carbon dioxide ($CO_2$) and water vapor ($H_2O$) are confirmed as two influential greenhouse gases (GHGs) existing in the biogeochemical system. The oceans are the dominant controlling factor to elucidate future climate scenarios. The oceans contain over 90% of the Earth's surface heat trapped by increased GHGs and absorb over 30% of the anthropogenic $CO_2$, most of which is from burning fossil fuels [1–3]. The measurement of GHGs emissions and energy exchange in temporal resolution is paramount to illuminating complex processes, especially important in coastal zones, where exceptionally heterogeneous terrestrial inputs, elemental cycling due to upwelling events (e.g., tides, currents, local land, or sea breeze), and exchanges between open and coastal ocean changes

induce a high dynamic variability of heat, water vapor, and carbon dioxide [4–6]. In the last two decades, there has been substantial efforts to examine the global budgets of many trace gases and energy via various disciplines and modeling studies at coastal seas [7–13]. However, one of the remaining challenges is to interpret and upscale relatively sparse measurements to a regional or continental scale in a coastal environment [14].

The eddy covariance (EC) method is currently the most direct, least empirical method used to access the temporal flux variability and atmospheric turbulence at local scale (1–10 km). Only with fast response (>10 Hz) and appropriate precision of the sensors has it become possible to resolve the fluctuations carried by small eddies in coastal regions where spatial and temporal variability of exchange rates are expected to be high.

Recent technology advances in laser spectroscopy have allowed the integrated EC system with a sonic anemometer to measure the flux densities. A $CO_2$/$H_2O$ sensor operating as a nondispersive infrared absorption (NDIR) device was firstly reported to measure sea-air $CO_2$ flux with open-path [15–17]. Improvements to the precision and accuracy of gas measurements were made with the occurrence of cavity-enhanced techniques. Cavity ring-down spectroscopy (CRDS [18]) and off-axis integrated-cavity output spectroscopy (OA-ICOS [19]) were developed and commercialized to measure $CO_2$/$H_2O$ fluxes with closed-path. Zahniser et al. firstly introduced a field deployment for eddy covariance employing a multi-pass absorption cell based on tunable diode laser spectroscopy (TDLAS) [20]. The available gas analyzer technology limits the measurements to areas of relatively complicated and ever-changing air–sea fluxes in marine boundary layers [21]. In more recent years, wavelength modulation spectroscopy (WMS) has been desirably used to resolve congested absorption features, enhance the signal to noise ratio (SNR), and discriminate $CO_2$ signals with overlapping signals of gaseous $H_2O$ due to its ability to suppress the low-frequency noise and resist the laser intensity fluctuation induced by scattering or vibration [22–24]. The scanned wavelength-modulation spectroscopy (scanned-WMS) and *1f*-normalized WMS-*nf* (WMS-*nf/1f*) method was more popular and demonstrated as stable and accurate under weak absorption conditions due to its low-frequency noise-rejection benefits [25,26]. However, the limited frequency modulation response ratio of laser diode restricts the applications with high time-resolution measurements, and the wavelength-dependent distortions resulting from etalon cavities/interferences restrict the applications in strong turbulent and harsh environment [27–30].

Yang et al. introduced a novel WMS-based first harmonic phase angle (θ*1f*) method (shortened to WMS-θ*1f*), which can make up for the high modulation frequencies or modulation depth limited conditions and achieved higher detection sensitivities [28,29]. Hanson et al. presented a detailed analysis of the scanned-wavelength WMS-θ*1f* gas sensing technique, made a performance comparison with scanned-wavelength WMS-*nf/1f* and scanned-wavelength direct-absorption spectroscopy [30]. WMS-θ*1f* exhibits improved measurement accuracy over the various WMS-*nf/1f* methods, especially for applications using long optical cavities (e.g., cavity-enhanced techniques).

In this work, we developed a compact open-path $CO_2$ and $H_2O$ sensor, and field-deployed it on the roof of the coastal monitoring station in Daya Bay, Shenzhen city. This sensor was designed to use two DFB lasers operating at ~2004 nm and ~1382 nm for high rate (500 Hz) atmospheric measurements based on the latest scanned-wavelength WMS-θ*1f* method. To our knowledge, this development is the first instrumentation of the new spectroscopic detection method and allows for new insights into GHG emission and flux measurements.

## 2. Materials and Methods

### 2.1. Instrument Design

The newly developed open-path, scanned-wavelength WMS-θ*1f* based $CO_2$ and $H_2O$ sensor is shown in Figure 1. It comprises a compact multi-pass Herriott cell [31], two stacked electronic boards for laser operation control, and data acquisition and processing, as well as a GPS module and an optical

module with reference gas cell. The design of the open-path cell combined a multi-pass and a single pass. Its dimensions were optimized for field portability with a $\Phi 120 \times 450$ mm sensor head and two 125 mm $\times$ 50 mm electronics units. The compact Herriott multi-pass cell, based on two concave mirrors (diameter: 50.8 mm, curvature radius: 400 mm) and a base length of 28 cm, achieved an optical path length of 20 m for $CO_2$ detection. The beam spot pattern was shown in the lower left corner of Figure 1. Each of the cell mirrors also possessed a small hole in the center region for 30-cm single-pass measurements of $H_2O$ by a second laser. The laser beam out of fiber was collimated by a gradient-index lens (Collimator 1) and entered through the center hole of the mirror, then received by the photodetector (PD 1) at the exit hole on the opposite cell mirror.
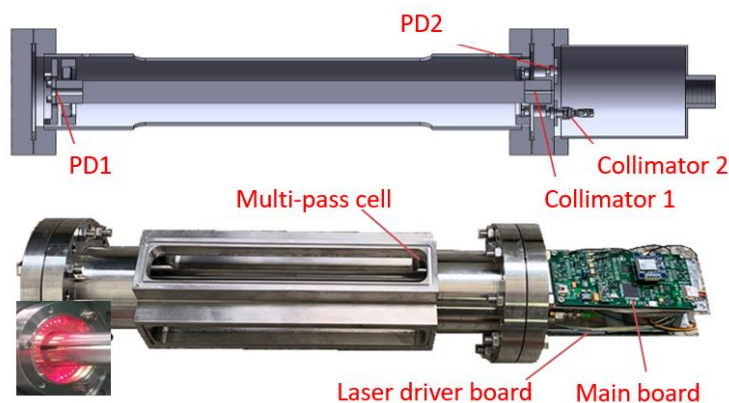


**Figure 1.** The assembled compact open-path atmospheric $CO_2$ and $H_2O$ sensor based on scanned-WMS-θ*1f* with lasers and drive electronics and main data acquisition and analysis electronics.

The diagram of the WMS-θ*1f*-based $CO_2$ and $H_2O$ detection system setup is depicted in Figure 2, including both the optical and electrical sub-systems. In the optical part, one Nanoplus continuous-wave distributed feedback (DFB) laser at ~2004 nm was used as the excitation laser source for $CO_2$ gas detection, and the other NEL DFB laser at ~1382 nm was employed for $H_2O$ vapor measurement. The 2004-nm laser output beam split into two light beams: one of them was coupled to the multi-pass gas cell, while the second beam was directed through a reference gas cell ($CO_2$ 442 ppm) for calibration purpose in programmed time intervals. Considering that it was difficult to maintain a water vapor reference cell in a field deployment environment, the structure of the open-path style sensor was designed with the possibility of mounting aluminum plates with O-ring seal on three sides to make the sensor air tight. This enables $H_2O$ measurement calibration via manual flowing reference $H_2O$ vapor into the multi-pass cell.

The electrical part includes the laser temperature and current controller shown in Figure 3a and the FPGA (field-programmable gate array) based signal acquisition and processing, analog lock-in demodulation shown in Figure 3b. Two lasers were tuned with a low-frequency scanning sinusoid and a high-frequency sinusoidal modulation generated by circuit based on an integrated 4-channel DDS (direct digital synthesizer, Analog Device, AD9959). The laser frequency scanning ranges were 1.3 cm$^{-1}$ for $CO_2$ measurements, and 1.2 cm$^{-1}$ for $H_2O$ vapor. The quadrature sinusoidal signals were synchronously generated after FPGA module sent 8-bits phase control-words to the independent DDS cores.
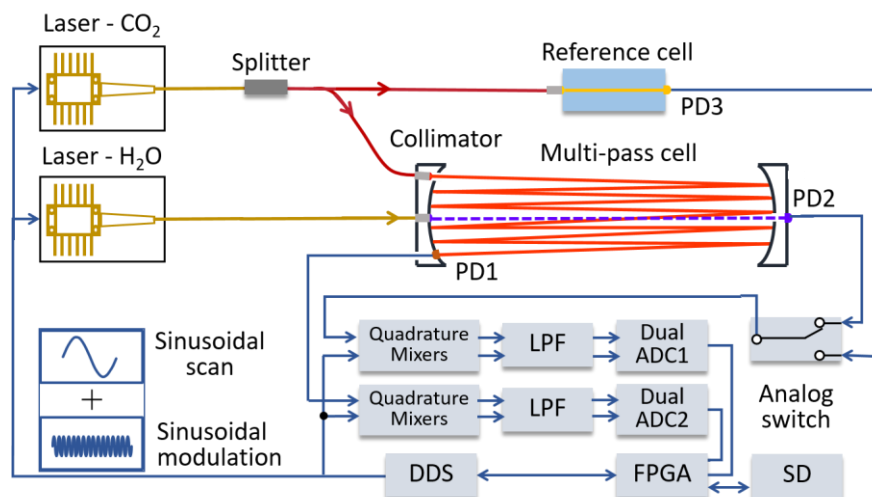
**Figure 2.** Diagram of the scanned-wavelength WMS-θ*1f* based $CO_2$ and $H_2O$ detection system, which consists of an open-path multi-pass cell and a reference gas cell for regular $CO_2$ auto-calibration. The field-programmable gate array-based (FPGA) lock-in detection used a direct digital synthesizer (DDS) to generate scanned-modulation laser driver current, demodulate the *1f* signal, calculate the gases concentration and store measurement results to a SD memory card. WMS, wavelength modulation spectroscopy.
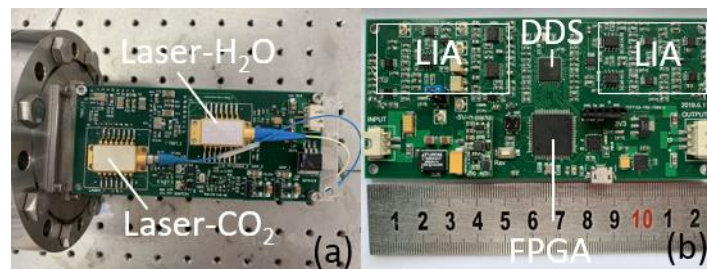


**Figure 3.** (**a**) The specially designed temperature and current control electronics to drive the two DFB lasers. (**b**) The DDS-based orthogonal analog lock-in amplifier (LIA) board to demodulate the WMS-*1f*-PA signal.

In typical WMS absorption measurements, the bandwidth of sensors scales with the modulation frequency. The tuning response and the controller circuit of laser and data acquisition bandwidth is usually what limits the modulation frequency used [26]. In general, a suitable, but complex, digital signal processor (DSP)-based digital lock-in amplifier (DLIA) and a software LabVIEW-based DLIA with more memorization elements, were used for harmonic signal extraction. However, the large amount of data needed to be processed limits the sampling frequency and the response, and makes DSP-based DLIA less practical in real-time high-data-rate systems. The large size and high power consumption of LabVIEW-based DLIA makes it is more suitable for laboratory measurements. For these reasons, a pair of orthogonal analog automatic lock-in amplifiers was implemented in this work to extract the X and Y components of the first harmonic signal.

The photodetectors' signal was processed by signal conditioning circuits with the low noise amplifiers and band-pass filters, and multiplied with the reference signal of measurement channel and 90° phase shifter channel separately. Then, the five-order Butterworth low pass filter (LPF) based on integrated operational amplifier cuts off frequency and reveals the mean value of the signal as DC component, whose peak-to-peak value is proportional to the concentration of gases to be measured. A dual-channel analog-to-digital convertor (ADC) (ADS8354, 16 bit, 1 MSPS) was used for simultaneous data sampling of the orthogonal harmonic spectral signal. To eliminate variable time-lag between

vertical wind and the gas density of interest, a miniature GPS module was operated by a microcontroller to track the real synchronous time at a 10 Hz update rate. The 500-Hz-fast raw sensor's measurement data and the GPS time were logged automatically to the on-board SD card for late use.

### 2.2. Spectroscopy Methodology

Scanned-wavelength-modulation spectroscopy (scanned-WMS), as an extension of TDLAS technique, can be used with any higher harmonic, modulation depth and has been applied to provide gas properties (e.g., concentration, temperature, pressure) in harsh environments because of its tolerance to noise [32]. In this method, the laser wavelength (or frequency) is simultaneously fast modulated at frequency $f_M$ and scanned at lower frequency $f_S$ sinusoidally over the absorption feature to obtain WMS spectra. When using a diode laser, this modulation is applied to its drive current. The corresponding laser intensity $I_0(t)$ and frequency $v(t)$ varies with injection current simultaneously:

$$I_0(t) = I_0(1 + i_s \cos(2\pi f_s t + \varphi_s) + i_M \cos(2\pi f_M t + \varphi_M)), \tag{1}$$

$$v(t) = v_0 + a_s \cos(2\pi f_s t) + a_M \cos(2\pi f_M t + \psi_M), \tag{2}$$

where $I_0$ and $v_0$ are the mean intensity and center optical frequency of the laser radiation; $i_S$ and $i_M$ are the relative intensity modulation (IM) amplitudes (normalized by $I_0$) of the scan and modulation components, respectively; $\varphi_S$ and $\varphi_M$ are the respective phase shift of the intensity scan and modulation; $a_S$ and $a_M$ are the relative frequency modulation (FM) amplitudes and $\psi_M$ is the phase shift of sinusoidal modulation. The transmission coefficient $\kappa(v)$ of monochromatic radiation through a gas medium is given by the Beer–Lambert law:

$$\kappa(v) = \left(\frac{I_t}{I_0}\right) = \exp(-\alpha(v)), \tag{3}$$

$$\alpha(v) = -P\chi_i L \sum_j S_j(T)\phi_j(v, T), \tag{4}$$

here $I_t$ is the transmitted intensity; $\alpha(v)$ represents the spectral absorbance, $P$ is the total gas pressure; $\chi_i$ is the mole fraction of the absorbing species; $L$ is path length; $T$ is the temperature; $S_j(T)$ and $\phi_j$ are the line-strength and the line-shape function of transition $j$. A similar model can be found in the literature, where Hanson et al. employs an approximation formula $1 - \alpha(v) \approx \exp(-\alpha(v))$ for weak absorption and expanded the expression in a Fourier cosine series [28,30,33]. The Fourier series of the spectral absorbance $\kappa(v)$ are given by:

$$\kappa(v) = \sum_{k=0}^{\infty} H_k(T, P, v_0, a_s, a_M, \psi_M)\cos(k\omega_M t) + \sum_{k=1}^{\infty} J_k(T, P, v_0, a_s, a_M, \psi_M)\sin(k\omega_M t), \tag{5}$$

here $\psi_M$ is the temporal phase offset (or time delay of response) between the laser diode current and light output. For the practical application, this phase delay manifests as a constant offset in the data time series for given laser and system settings. The time delay is assumed to be zero here to simplify the analysis expression. The $k^{th}$ order Fourier coefficients are listed below:

$$H_0(T, P, v_0, a_s, a_M) = \frac{P\chi_i L}{2\pi} \int_{-\pi}^{\pi} \exp\left[-\sum_j S_j(T)\phi_j(v_0 + a_s\cos(\eta_s\theta) + a_M\cos(\theta))\right]d\theta, \tag{6}$$

$$H_{k\neq 0}(T, P, v_0, a_s, a_M) = \frac{P\chi_i L}{\pi} \int_{-\pi}^{\pi} \exp\left[-\sum_j S_j(T)\phi_j(v_0 + a_s\cos(\eta_s\theta) + a_M\cos(\theta))\right]\cos(k\theta)d\theta, \tag{7}$$

$$J_{k \neq 0}(T, P, v_0, a_s, a_M) = \frac{P \chi_i L}{\pi} \int_{-\pi}^{\pi} \exp\left[-\sum_j S_j(T)\phi_j(v_0 + a_s \cos(\eta_s \theta) + a_M \cos(\theta))\right] \sin(k\theta)d\theta, \quad (8)$$

where $\eta_s = \omega_S / \omega_M$ with $\omega_S = 2\pi f_S$, $\omega_M = 2\pi f_M$. $H_0$ is equivalent to transmission coefficient at center frequency $v_0$. $H_k$ and $J_k$ are related to the $k^{th}$ derivative of transmission coefficient function. The *1f* component is demodulated by means of multiplication of detector signal with the orthogonal sinusoidal reference signal at $f_M$:

$$X_{1f} = \frac{I_0}{2}\left(i_M \cos \varphi_M - i_M H_0 \cos \varphi_M - H_1 - \frac{1}{2}i_M H_2 \cos \varphi_M - \frac{1}{2}i_M J_2 \sin \varphi_M\right), \quad (9)$$

$$Y_{1f} = -\frac{I_0}{2}\left(i_M \sin \varphi_M - i_M H_0 \sin \varphi_M + J_1 + \frac{1}{2}i_M H_2 \sin \varphi_M + \frac{1}{2}i_M J_2 \cos \varphi_M\right), \quad (10)$$

The first harmonic phase angle $\theta_{1f}$ can be calculated from Equations (9) and (10):

$$\theta_{1f} = \arctan\left(\frac{Y_{1f}}{X_{1f}}\right) = \arctan\left(\tan(-\varphi_M)\frac{1 - H_0 + \frac{J_1}{i_M \sin \varphi_M} + \frac{H_2}{2} + \frac{J_2 \sin \varphi_M}{2 \cos \varphi_M}}{1 - H_0 - \frac{H_1}{i_M \cos \varphi_M} - \frac{J_2}{2} - \frac{H_2 \sin \varphi_M}{2 \cos \varphi_M}}\right), \quad (11)$$

with the laser average incident intensity $I_0$ being canceled out, $\theta_{1f}$ only depends on the Fourier coefficient ($H_0$, $H_{k \neq 0}$, $J_{k \neq 0}$), the linear amplitude ($i_M$) and the phase shifts ($\varphi_M$) between IM and FM. In general, $H_0$ is typically much smaller than 1, $H_2 \ll H_1$ and $J_2 \ll J_1$ in Equation (11). $\theta_{1f}$ signals respond to the dominant contributor of $H_1$ and $J_1$, leading to a linear proportion to the concentration of absorbing species. When the absorption is zero, the $H_0$ term is equal to 0, and $H_{k \neq 0}$ and $J_{k \neq 0}$ equal to 0, which leads to $\theta_{1f}^0 = -\varphi_M$.

## 3. Results and Discussion

### 3.1. Instrument Performance

The performance of WMS sensors is commonly evaluated with the detection limits by quantifying noise-equivalent absorbance (NEA). The optimal modulation depth is chosen for the maximized signal-to-noise (SNR) of the WMS-*nf* signal at absorption line center. For our developed sensor, the rate of the spectral and concentration measurements equals the sinusoidal scanning rate around 2 kHz. During the experiment, the modulation frequency was varied from 350 kHz to 600 kHz, while the modulation amplitude changes from 8 mA to 50 mA. The peak values of $\theta_{1f}$ phase signal measured for $CO_2$ and $H_2O$ vapor spectral absorption determinations are plotted in Figure 4. Average standard deviation of the peak-to-peak values of $\theta_{1f}$ with respect to the different modulation conditions was 1.3% for $CO_2$ and 2.0% for $H_2O$. As signal noise varied as well, the maximum SNR occurred at around a modulation amplitude of 45 mA and modulation frequency of 450 kHz, for both the 2004-nm laser for $CO_2$ detection and for the 1382-nm laser for $H_2O$ vapor detection. The corresponding laser frequency modulation depths were 0.33 cm$^{-1}$ for 2004-nm laser and 0.42 cm$^{-1}$ for 1382-nm laser, respectively.
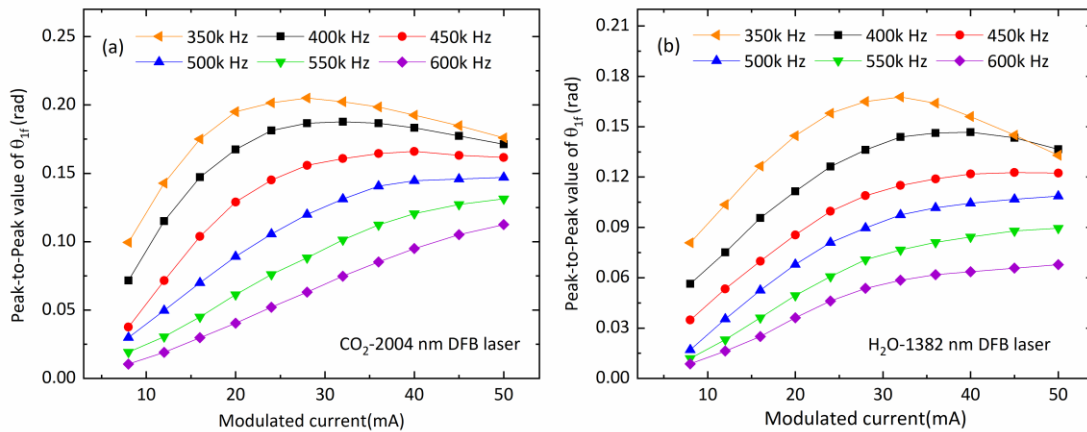
**Figure 4.** Dependence of the measured peak-to-peak values of $\theta_{1f}$ phase signal on modulation amplitudes and frequencies applied to diode lasers for (**a**) $CO_2$ spectral line and (**b**) $H_2O$ vapor spectral line.

In order to avoid overlapping interferences caused by high-order harmonics between the scanning and modulation frequencies, they were adjusted to avoid being an integer multiple. Figure 5 presents the photodetector signals with and without spectral absorption when the laser was scan-modulated with a scan frequency $f_S = 1.97$ kHz and modulation frequency $f_S = 449.3$ kHz.
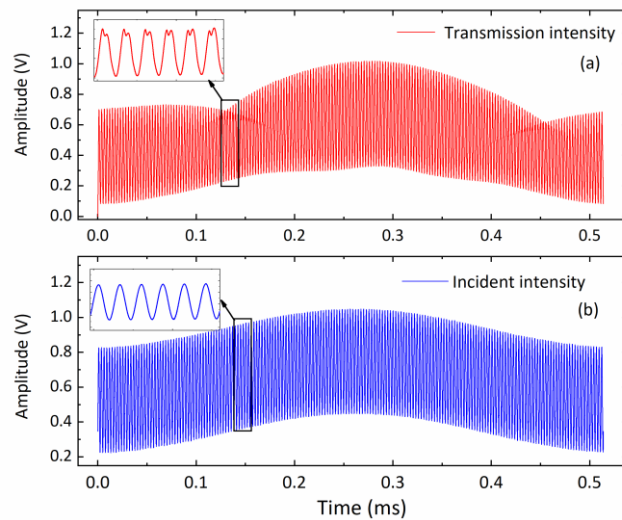


**Figure 5.** An example of measured photodetector signals in a scanned-WMS experiment: (**a**) transmission intensity profile after spectral absorption, and (**b**) the incident laser intensity profile. The injection current of the laser was scanned at 1.97 kHz and modulated at 449.3 kHz with the modulation amplitude of 50 mA. The subpanels show the absorption and modulation envelopes in detail.

Figure 6 shows the frequency spectrum of the measured scanned-WMS detector signal in logarithmic scale. The magnitudes of the higher modulation harmonic frequency components decreased rapidly. The *1f* signal is one order-of-magnitude bigger than the *2f* ones. Both analog and digital filtering were applied to extract the *1f* signal component. In this case, a 42 kHz analog 5th-order Butterworth filter (following the lock-in amplifier) was sufficient to extract the scanned WMS-θ*1f* signal. After ADC processing, the numerical data was sent to FPGA, filtered by a digital finite-impulse-response (FIR) low-pass filter at 4 kHz with a hamming window. The peak-to-peak value of first harmonic phase angle (during the down-scan period) was then calculated and used late for the spectral absorption calculation. An example of such a scanned-WMS-θ*1f* signal at a scan

repetition rate of 1.97 kHz is shown in Figure 7. There are slight differences in up-scan and down-scan due to the phase-shift between the laser intensity and wavelength scanning.
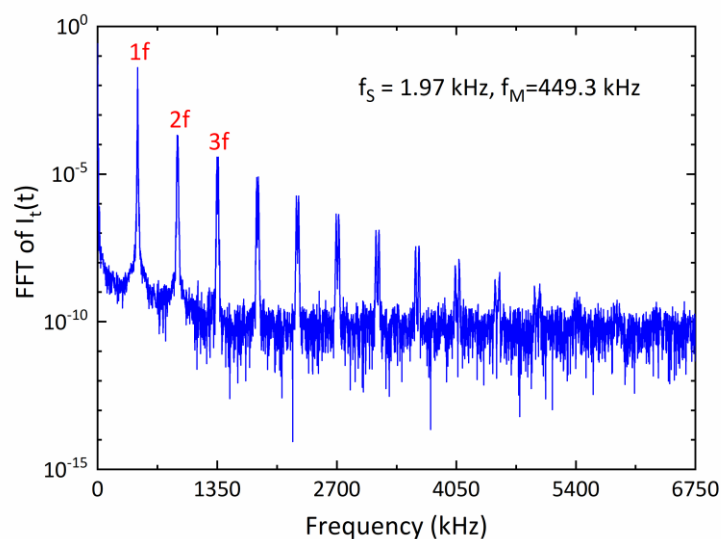


**Figure 6.** Frequency spectrum of a measured detector signal in a scanned-WMS experiment. The first three harmonic signals are marked in the picture where *1f* = ~450 kHz, *2f* = ~900 kHz, and *3f* = ~1350 kHz.
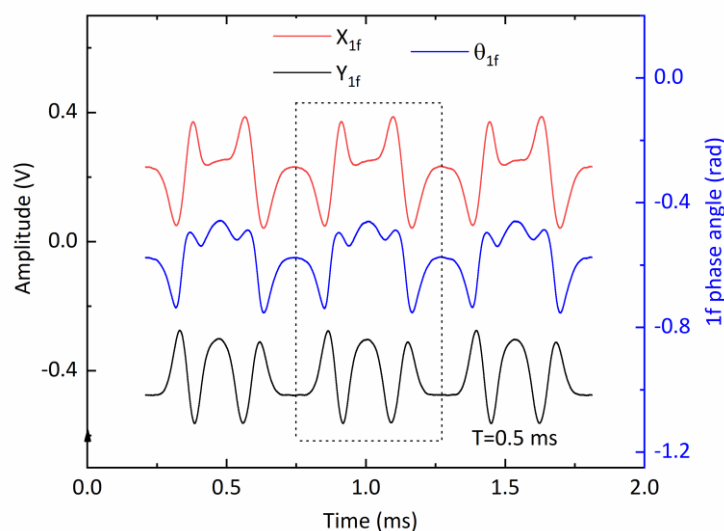


**Figure 7.** The extractions of the first harmonic signals via anlage quadrature lock-in amplifiers and the calculated first harmonic phase angle. The dotted box indicates a single scan period.

### 3.2. Calibration and Measurement Precision

To investigate linearity of the open-path sensor's concentration measurements, a series of experiments were performed. The $CO_2$ standard gas balanced by $N_2$ ranging from 0 ppm to 680 ppm was filled into the enclosed optical cell at a flow rate of 2 L/min. The $H_2O$ mixing ratio generated by a calibrated gas dilution (HovaCAL digital 311-MF, IAS GmbH) ranging from 1.2% to 3.4%, which covered the typical humidity of the coastal area where we did our field measurements. The measured peak-to-peak results of $\theta_{1f}$ signal and the respective concentrations were recorded under ambient temperature and pressure, and illustrated in Figure 8a,b. The error bars denote the respective standard deviations (1σ) of the individual 10-min averages of measured gas concentration. The maximum of deviations was found to be 0.27% of the measured $CO_2$ concentration at 150 ppm and 4.01% for the $H_2O$ concentration at 3.4%. Good linear correlations were observed with a correlation

coefficient of 0.997 for $CO_2$ and 0.999 for $H_2O$, which can be used for calibration of the measured peak-to-peak values of $\theta_{1f}$ signal to the corresponding concentration.
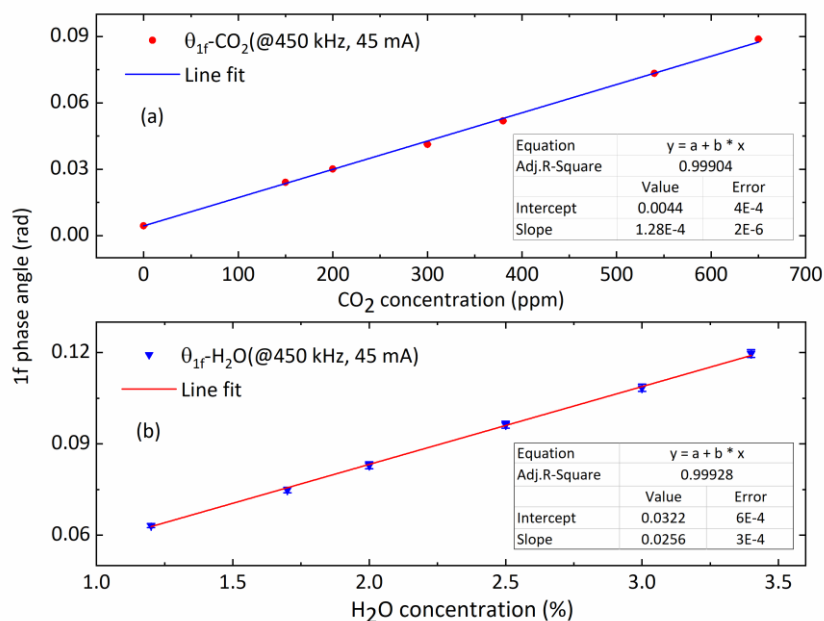


**Figure 8.** Calibration measurements of the peak-to-peak magnitude of the *1f* phase angle $\theta_{1f}$ at various reference gas concentrations of (**a**) $CO_2$ and (**b**) $H_2O$ vapor. Their good linear dependence is confirmed by the straight-line fit (solid line) with details shown in the legend.

Allan deviation analyses were performed on $CO_2$ and $H_2O$ measurements to determine the system stability and the optimal averaging time and detection limits [34]. Figure 9 shows the Allan deviation analysis of measurement stability for $CO_2$ and $H_2O$ vapor, with a sample mixing ratio of 42 ppm $CO_2$ and 1200 ppm $H_2O$. The sample gas was flowed (200 mL/min) through the sensor with its side aluminum enclosure plates mounted. The concentration measurements were conducted in the laboratory at a fast output data rate of 500 Hz. This corresponds to a high time resolution of 2 ms. The precision at 500 Hz data rate was 0.31 ppm for $CO_2$, and 8.35 ppm for $H_2O$. Data averaging helped to improve the measurement precision. A minimum detection limit of 62 ppb $CO_2$ was achieved with an integration time of ~0.06 s, and 0.89 ppm $H_2O$ for an integration time of ~0.26 s.
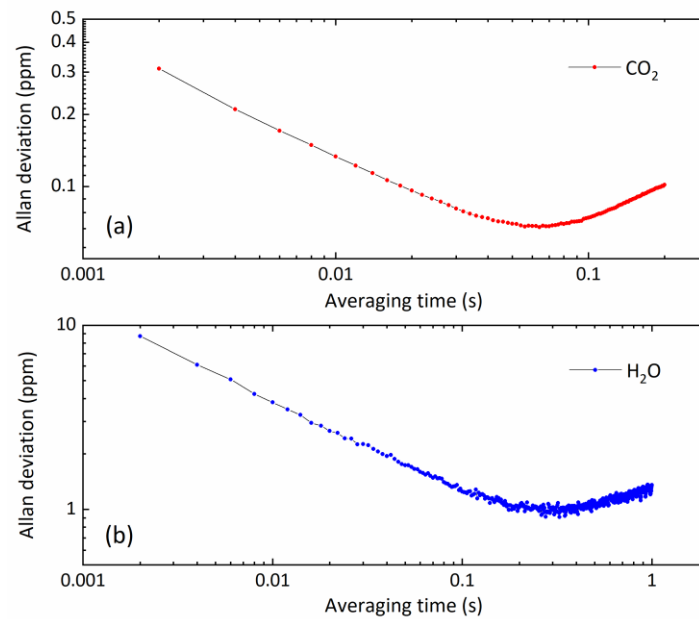
**Figure 9.** Allan deviation analysis of measurement stability of gas flow at a data rate of 500 Hz: (**a**) 42 ppm $CO_2$ and (**b**) 1200 ppm $H_2O$.

### 3.3. Comparison and Field Measurements

After experimentally verifying the accuracy and stability of the 500-Hz-fast scanned-WMS-θ1f instrument was adequate for eddy covariance application, two sets for short and longer time of comparison measurements together with a commercial open-path infrared gas analyzer (model LI-7500A; LI-COR Inc.2019 [35]) were performed. These measurement results are displayed in Figures 10 and 11, respectively. The 1-s comparison measurements in Figure 10 show very good $CO_2$ and $H_2O$ concentration agreement between our scanned-WMS sensor and the LI-7500A analyzers. LI-7500A made measurement at a data rate of 20 Hz, whereas our scanned-WMS sensor was able to do the measurements at a much faster rate of 500 Hz. The high data rate of our compact scanned-WMS sensor was able to reveal rapid changes in turbulent environments and was essential for eddy covariance applications.

The second set of comparison measurements between the two systems were conducted at a local field site. The data and analysis displayed in Figure 11 is for a 10-min data segment. For eddy covariance flux applications, data length of similar duration or longer is required to meet the criteria of stationary flux dynamic environment [36]. The time-series of $CO_2$ and $H_2O$ observations by the two techniques present a consistent trend, as shown in Figure 11a,c, respectively. The reason for some measurement difference in measurements between the two instruments was that they were placed at a distance in order to avoid affecting the air flow on each other.
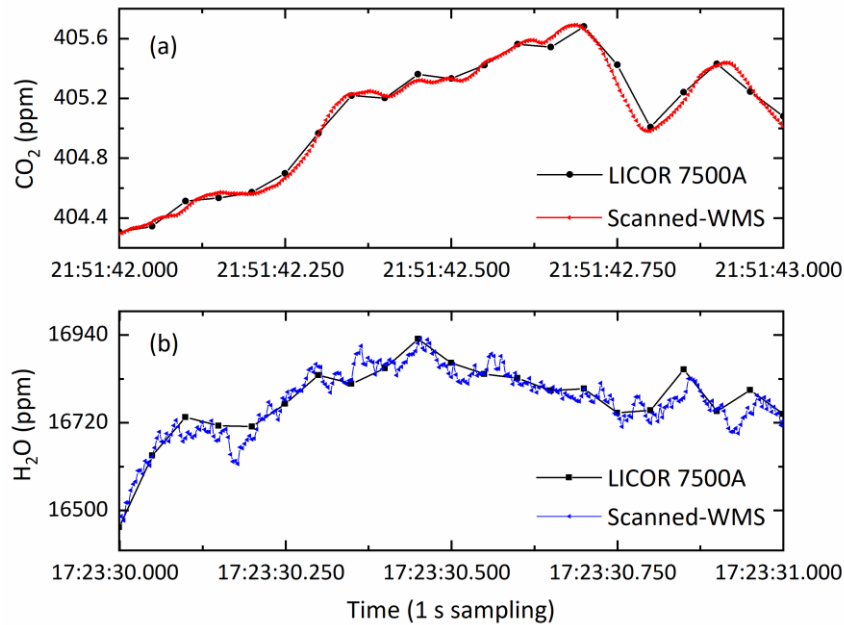
**Figure 10.** Examples of a 1-s comparison measurements of (**a**) $CO_2$ and (**b**) $H_2O$ show detailed results by the scanned-WMS sensors (at 500 Hz data rate) and LI-7500A (at 20 Hz).
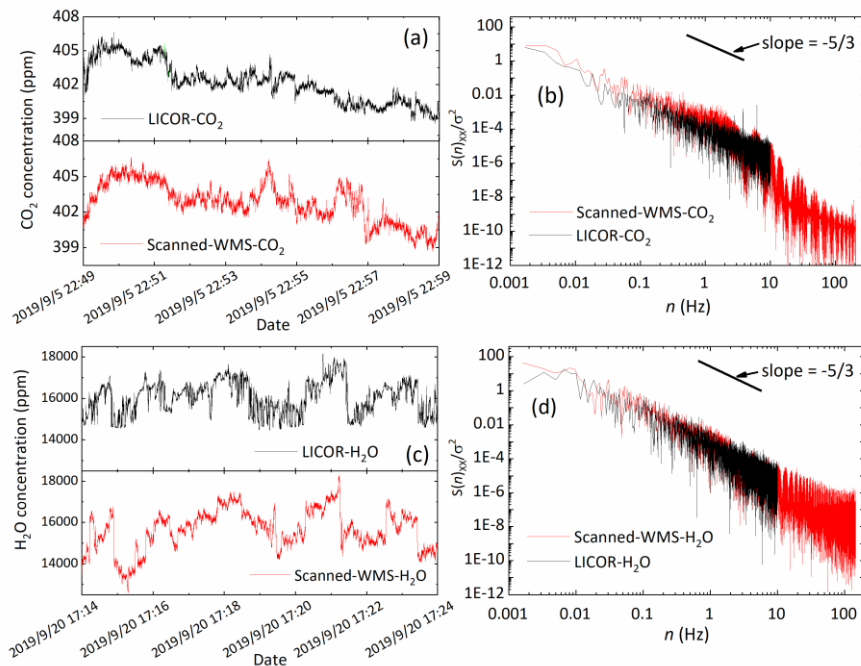


**Figure 11.** Comparison measurements by our scanned-WMS-$\theta 1f$ sensor and a LICOR instrument over a duration of 10 min. (**a**) $CO_2$ measurements and (**b**) the corresponding power spectra; (**c**) $H_2O$ measurements and (**d**) the corresponding power spectra.

To assess the ability of the gas analyzer to measure turbulent activities across certain frequency ranges, the normalized power spectral densities of the temperature and concentration results of $CO_2$ and $H_2O$ with different data rates were plotted against frequency in Figure 11b,d. In the low frequency region below 1 Hz, all three spectra fall with a slope of approximate $-5/3$. As our scanned-WMS-$\theta 1f$ sensor operated at 500 Hz fast data rate, it was able to reveal the presence of turbulence at high frequency of 10~100 Hz.

Our open-path $CO_2$/$H_2O$ sensor had been field deployed atop a 48-m shore-based monitoring station (22°32′N, 114°35′W) located in Yangmeikeng, on the windward of Daya Bay, Shenzhen. A photograph of the sensor installation is shown in Figure 12. The stand-alone sensor was able to make continuous long-term measurements. The LI-7500A analyzer was also installed nearby to conduct comparison measurements. The real-time atmospheric temperature, pressure, and relative humidity at the installation site were recorded with an integrated PHT sensor (MS8607, MEAS).



**Figure 12.** A photograph of the scanned-WMS-θ*1f* instrumental set-up.

The experiment began on September 12 and lasted 15 days as illustrated by Figure 13. The $H_2O$ concentrations obtained from the two instruments are shown in Figure 13b and the corresponding temperature fluctuation is shown in Figure 13a. As a coastal city, the atmospheric flow is subjected to the influence of subtropical oceanic monsoons. In September, the moist air masses mainly from the South China Sea brought abundant rainfall. The LICOR sensor registers some erroneous values during September 13–18 and need post-field correction. Results of both instruments were consistent, while our instrument provided much high temporal resolution with its 500 Hz data rate.

The partial pressure of $H_2O$ vapor in the ocean atmosphere is relatively higher in general and ranges from 1% to 3.5%. The diurnal air temperature and $H_2O$ partial pressure shows regular fluctuating levels, indicating that the land-sea breeze is formed with upward heat flux and the temperature difference between land and sea in the reversal time, which is consistent with the previous research. The field measurement results demonstrate that the open-path scanned-WMS-θ*1f* sensor is capable of performing high time resolution and long-term field measurements to capture various GHG emissions. Future work will be to measure eddy covariance $CO_2$/$H_2O$ flux, latent heat, and sensible heat measurements integrated with sonic anemometer.
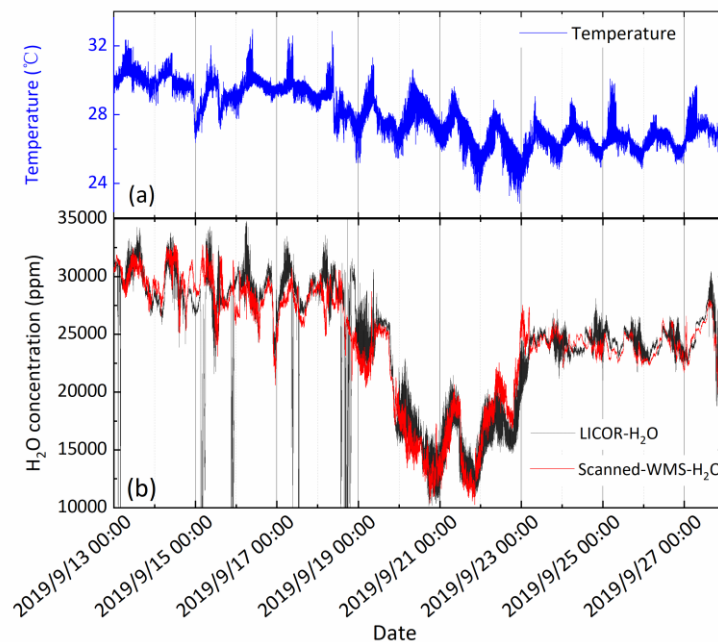
**Figure 13.** (**a**) Temperature data series over half a month period and (**b**) a comparison of atmospheric $H_2O$ vapor data series from LICOR analyzer and our scanned-WMS-$\theta 1f$ sensor over the same time period.

## 4. Conclusions

In this paper, we presented a compact, diminutively integrated, field-deployable, open-path $CO_2/H_2O$ sensor based on the newly invented scanned-wavelength modulation spectroscopy with $\theta 1f$ phase detection method. The system was installed on top of a coastal monitoring station for a long-term inter-comparison with existing commercial, atmospheric $CO_2/H_2O$ instrument (LICOR 7500A). The sensor employed a configuration of dual optical path arrangement combining a compact multi-pass gas cell of 20 m path-length for $CO_2$ detection, and a 30 cm single pass for $H_2O$ measurement. Two DFB laser diodes were used as the optical sources (~2004 nm for $CO_2$; 1382 nm for $H_2O$) in the scanned-WMS-$\theta 1f$ based sensor host. The open-path $CO_2$ and $H_2O$ gas analyzer has a sensitivity of 62 ppb (averaging time 60 ms) and 0.89 ppm (averaging time 0.27 s), comparable to other widely used $CO_2/H_2O$ sensors. One outstanding advantage of our newly developed sensor is its fast (500 Hz) time resolution, which is able to capture transient $CO_2/H_2O$ fluctuations.

**Author Contributions:** X.L. and B.C. conceived and designed the experiments; C.Y. provided the methodology; R.K. and L.S. supervised the project; F.Y. and M.H. contributed analysis tools; X.L. performed the experiments, analyzed the data, and drafted the paper; Y.H. reviewed and edited the paper. All authors have read and agreed to the published version of the manuscript.

**Conflicts of Interest:** The authors declare no conflicts of interest.

## References

1. Tans, P.P.; Bakwin, P.S.; Guenther, D.W. A feasible Global Carbon Cycle Observing System: A plan to decipher today's carbon cycle based on observations. *Glob. Chang. Boil.* **1996**, *2*, 309–318. [CrossRef]
2. Takahashi, T.; Sutherland, S.C.; Sweeney, C.; Poisson, A.; Metzl, N.; Tilbrook, B.; Bates, N.; Wanninkhof, R.; Feely, R.A.; Sabine, C.; et al. Global sea–air CO2 flux based on climatological surface ocean pCO2, and seasonal biological and temperature effects. *Deep. Sea Res. Part II Top. Stud. Oceanogr.* **2002**, *49*, 1601–1622. [CrossRef]

3.  Pachauri, R.K.; Meyer, L.A. (Eds.) *Climate Change 2014: Synthesis Report. Contribution of Working Groups I, II and III to the Fifth Assessment Report of the Intergovernmental Panel on Climate Change*; IPCC: Geneva, Switzerland, 2014; 151p.

4.  Muller-Karger, F.E.; Varela, R.; Thunell, R.; Luerssen, R.; Hu, C.; Walsh, J.J. The importance of continental margins in the global carbon cycle. *Geophys. Res. Lett.* **2005**, *32*. [CrossRef]

5.  Pachauri, R.K.; Reisinger, A. (Eds.) *Climate Change 2007: Synthesis Report*; Intergovernmental Panel on Climate Change: Cambridge, UK, 2007.

6.  Crawford, T.L.; Mcmillen, R.T.; Meyers, T.P. Spatial and temporal variability of heat, water vapor, carbon dioxide, and momentum air-sea exchange in a coastal environment. *J. Geophys. Res.* **1993**, *98*, 12869–12880. [CrossRef]

7.  Edson, J.B.; Fairall, C.W.; Mestayer, P.G.; Larsen, S.E. A study of the inertial-dissipation method for computing air-sea fluxes. *J. Geophys. Res. Space Phys.* **1991**, *96*, 10689. [CrossRef]

8.  Hendriks, D.M.D.; Dolman, H.; Van Der Molen, M.; Van Huissteden, J. A compact and stable eddy covariance set-up for methane measurements using off-axis integrated cavity output spectroscopy. *Atmos. Chem. Phys. Discuss.* **2008**, *8*, 431–443. [CrossRef]

9.  Takahashi, T.; Sutherland, S.C.; Wanninkhof, R.; Sweeney, C.; Feely, R.A.; Chipman, D.W.; Hales, B.; Friederich, G.; Chavez, F.; Sabine, C.; et al. Climatological mean and decadal change in surface ocean pCO2, and net sea–air CO2 flux over the global oceans. *Deep. Sea Res. Part II: Top. Stud. Oceanogr.* **2009**, *56*, 554–577. [CrossRef]

10. Prytherch, J.; Yelland, M.; Pascal, R.W.; Moat, B.I.; Skjelvan, I.; Neill, C.C. Direct measurements of the CO2flux over the ocean: Development of a novel method. *Geophys. Res. Lett.* **2010**, *37*, 12. [CrossRef]

11. Baldocchi, D. Measuring fluxes of trace gases and energy between ecosystems and the atmosphere—The state and future of the eddy covariance method. *Glob. Chang. Biol.* **2014**, *20*, 3600–3609. [CrossRef]

12. Honkanen, M.; Laakso, L.; Tuovinen, J.P. Measuring turbulent CO2 fluxes with a closed-path gas analyzer in a marine environment. *Atmos. Meas. Tech.* **2018**, *11*, 5335–5350. [CrossRef]

13. Roobaert, A.; Laruelle, G.G.; Landschützer, P. The spatiotemporal dynamics of the sources and sinks of CO2 in the global coastal ocean. *Glob. Biogeochem. Cycles* **2019**, *33*. [CrossRef]

14. Fennel, K.; Alin, S.; Barbero, L.; Evans, W.; Bourgeois, T.; Cooley, S.; Dunne, J.; Feely, R.A.; Hernandez-Ayon, J.M.; Hu, X.; et al. Carbon cycling in the North American coastal ocean: A synthesis. *Biogeosciences* **2019**, *16*, 1281–1304. [CrossRef]

15. Jones, E.P.; Smith, S.D. A first measurement of sea-air CO2 flux by eddy correlation. *J. Geophys. Res.* **1977**, *82*. [CrossRef]

16. Brach, E.J.; Desjardins, R.L.; Amour, G.T.S. Open path CO2 analyzer. *J. Phys. E* **1981**, *14*, 1415–1419. [CrossRef]

17. Ohtaki, E.; Matsui, T. Infrared device for simultaneous measurement of fluctuations of atmospheric carbon dioxide and water vapor. *Bound.-Layer Meteorol.* **1982**, *24*, 109–119. [CrossRef]

18. He, Y.; Jin, C.; Kan, R.; Liu, J.; Liu, W.; Hill, J.; Jamie, I.; Orr, B.J. Remote open-path cavity-ringdown spectroscopic sensing of trace gases in air, based on distributed passive sensors linked by km-long optical fibers. *Opt. Express* **2014**, *22*, 13170–13189. [CrossRef] [PubMed]

19. O'Keefe, A.; Scherer, J.J.; Paul, J.B. cw Integrated cavity output spectroscopy. *Chem. Phys. Lett.* **1999**, *307*, 343–349. [CrossRef]

20. Zahniser, M.S.; Nelson, D.D.; McManus, B.; Kebabian, P.L.; Lloyd, D.; McManus, J.B. Measurement of trace gas fluxes using tunable diode laser spectroscopy. *Philos. Trans. R. Soc. London. Ser. A Phys. Eng. Sci.* **1995**, *351*, 371–382.

21. Rowe, M.; Fairall, C.W.; Perlinger, J.A. Chemical sensor resolution requirements for near-surface measurements of turbulent fluxes. *Atmos. Chem. Phys. Discuss.* **2011**, *11*, 5263–5275. [CrossRef]

22. Li, H.; Rieker, G.B.; Liu, X. Extension of wavelength-modulation spectroscopy to large modulation depth for diode laser absorption measurements in high-pressure gases. *Appl. Opt.* **2006**, *45*, 1052–1061. [CrossRef]

23. Rieker, G.B.; Jeffries, J.B.; Hanson, R.K. Calibration-free wavelength-modulation spectroscopy for measurements of gas temperature and concentration in harsh environments. *Appl. Opt.* **2009**, *48*, 5546–5560. [CrossRef] [PubMed]

24. Mei, L.; Svanberg, S. Wavelength modulation spectroscopy-digital detection of gas absorption harmonics based on Fourier analysis. *Appl. Opt.* **2015**, *54*, 2234–2243. [CrossRef] [PubMed]

25. Strand, C.L. Scanned Wavelength Modulation Absorption Spectroscopy with Application to Hypersonic Impulse Flow Facilities. Ph.D. Thesis, Stanford University, Stanford, CA, USA, 2014.

26. Goldenstein, C.S.; Almodóvar Christopher, A.; Jeffries, J.B. High-bandwidth scanned-wavelength-modulation spectroscopy sensors for temperature and H2O in a rotating detonation engine. *Meas. Sci. Technol.* **2014**, *25*, 105104. [CrossRef]

27. Wang, Z.; Fu, P.; Chao, X. Laser Absorption Sensing Systems: Challenges, Modeling, and Design Optimization. *Appl. Sci.* **2019**, *9*, 2723. [CrossRef]

28. Yang, C.; Mei, L.; Kan, R. Wavelength modulation spectroscopy by employing the first harmonic phase angle method. *Opt. Express* **2019**, *27*, 12137–12146. [CrossRef] [PubMed]

29. Yang, C.; Mei, L.; Wang, X.P.; He, Y.B.; Kan, R.F. Simultaneous measurement of gas absorption and path length by employing the first harmonic phase angle method in wavelength modulation spectroscopy. *Opt. Express* **2020**, *28*, 3289–3297. [CrossRef]

30. Peng, W.Y.; Strand, C.L.; Hanson, R.K. Analysis of laser absorption gas sensors employing scanned-wavelength modulation spectroscopy with 1f-phase detection. *Appl. Phys. B Opt. Lasers* **2019**. [CrossRef]

31. Herriott, D.R.; Schulte, H.J. Folded Optical Delay Lines. *Appl. Opt.* **1965**, *4*, 883–889. [CrossRef]

32. Goldenstein, C.S.; Schultz, I.A.; Spearrin, R.M.; Hanson, R.K. Scanned-wavelength-modulation spectroscopy near 2.5 µm for H2O and temperature in a hydrocarbon-fueled scramjet combustor. *Appl. Phys. B Opt. Lasers* **2014**, *116*, 717–727. [CrossRef]

33. Zhou, Y.Z. Development of a Single-Ended Laser-Absorption Spectroscopy Sensor for High-Temperature Gases. Ph.D. Thesis, Purdue University, West Lafayette, IN, USA, 2018.

34. Werle, P.; Šlemr, F. The limits of signal averaging in atmospheric trace-gas monitoring by tunable diode-laser absorption spectroscopy (TDLAS). *Appl. Phys. A* **1993**, *57*, 131–139. [CrossRef]

35. LI-COR, Inc. *LI-7500RS Open-Path CO2/H2O Gas Analyzer Instruction Manual*; LI-COR Biosciences: Lincoln, NE, USA, 2019.

36. Kaimal, J.C.; Wyngaard, J.C.; Izumi, Y.; Coté, O.R. Spectral characteristics of surface-layer turbulence. *Q. J. R. Meteorol. Soc.* **1972**, *98*, 563–589. [CrossRef]